Supporting Information

Near Infrared Vibrational Second Harmonic Generation: a New Nonlinear Interfacial Vibrational Spectroscopy

Somaiyeh Dadashi, Ziyad Thekkayil, and Eric Borguet*.

Department of Chemistry, Temple University, Philadelphia, PA, USA

* Corresponding author: eborguet@temple.edu

Keywords: Vibrational second harmonic generation, vibrational sum frequency generation, anharmonicity, dissociation energy, Al_2O_3, acetonitrile, chloroform, overtones.

1. Optical setup

The steady-state near infrared vibrational second harmonic generation (NIR-vSHG), near infrared vibrational sum frequency generation (NIR-vSFG) and mid infrared vibrational sum frequency generation (MIR-vSFG) experiments were performed using a tunable broadband IR beam and a narrowband visible beam. 10% of the output of a femtosecond laser (Coherent, Monaco 1035-80-60 Series II), emitting pulses with a variable repetition rate (7-750 kHz) centered at 1035 nm, and pulse width of 260 fs, is used as the visible beam. The bandwidth of the visible beam is reduced from 7.7 nm to ~2.5 nm using a band pass filter (Omega Optical, Inc.: 1035BP2). Approximately 90% of the Monaco output pumps a commercial optical amplifier (OPA: Light Conversion, Opera-HP) to generate tunable MIR pulses in the 2-5 μm (spectral width ~150 – 200 cm^{-1} FWHM, Figure S3b,d), as well as 1045-2600 nm NIR beam (spectral width ~100 cm^{-1} FWHM, Figure S3f).

The visible (using a 400 mm planoconvex lens) and IR (using a 150 mm planoconvex lens) beams were spatially and temporally overlapped at the sample interface to generate sum frequency (SF) light. The incident angles at the interface were 60°: IR and 54°: Visible with

~100 and ~140 μm spot sizes, respectively. The MIR experiments were conducted using 7.5 kHz repetition rates, with pulse energies ~2 μJ (visible), ~0.2 μJ (IR, OH region), and ~0.3 μJ (IR, CH region), while the NIR experiments were conducted using 107 kHz repetition rates, with pulse energies ~2 μJ (visible), ~1.2 μJ (NIR, OH region), and ~1 μJ (NIR, CH region). The vSFG spectra of mica exhibits an azimuthal angle dependence,[1] and so all the spectra we report were taken after rotating mica to the azimuthal angle giving the maximum vSFG intensity. The resulting vSFG and NIR-vSHG responses were separated from the 1035 nm visible beam using a 950 nm short pass filter, and collected via a charge-coupled device detector (Princeton Instruments: PIXIS 1024BX-SH) coupled to a spectrograph (Princeton Instruments: HRS300S), integrating for acquisition times of 60 s. The spectra were normalized to the IR/NIR pulse spectral profiles at the respective frequencies, acquired by using a gold coated alumina window (MIR)/ quartz (NIR) at the sample position.

2. Materials

As-received acetonitrile and chloroform (HPLC Grade, Fisher Chemicals), acetonitrile-d_3 (D, 99.8%) and chloroform-d (D, 99.96%) (Cambridge Isotope Laboratories), c-cut Al_2O_3 equilateral roof prism (α-Al_2O_3(0001), from Team Photon Inc., San Diego, CA), and 001 oriented muscovite mica (25 x 25 x 0.1 mm, Ted Pella, Inc.) were used for the experiments. The alumina prism was cleaned using Piranha solution (1:3, H_2O_2: H_2SO_4) for ~ 60 minutes in a Teflon dish and was rinsed with deionized water (>18.2 MΩ.cm, ThermoScientific Barnstead EasyPure II purification system with UV lamp) to remove residual piranha. (*CAUTION: piranha is extremely reactive and can cause severe damage to skin/eyes. Handle using gloves, goggles, a lab coat, and extreme care.)* The sample was then dried using ultra high purity N_2 gas. At the end of the cleaning process, the homemade sample holder, Teflon spacer and the prism were plasma cleaned (low-pressure RF plasma: Harrick PDC-32G) for ~ 2 minutes. A 001 oriented muscovite mica (25 x 25 x 0.1 mm, Ted

Pella, Inc.) sheet was cleaved using a clean razor blade or scotch tape prior to the experiments in a uniform direction to minimize flakes and defects on the surface of the mica. The same mica was used for all the experiments reported in this study.

3. Harmonic potential and Morse potential

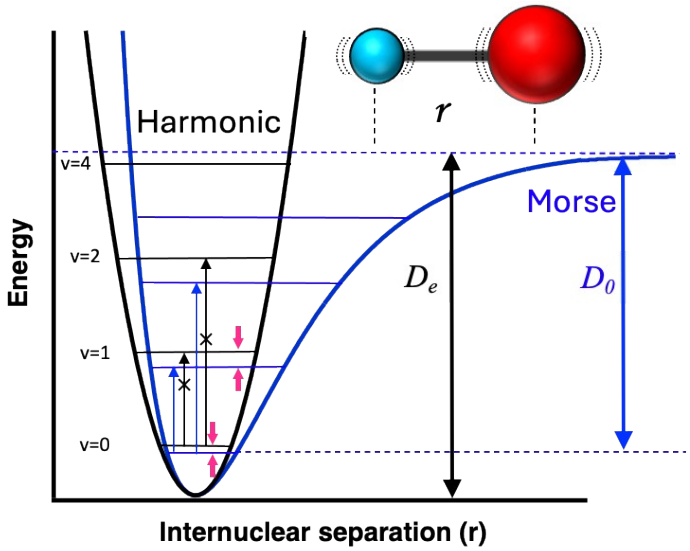

Figure S1: The harmonic potential and the Morse potential. The Morse potential (blue curve) accurately models the dissociation energies D_e (indicating the energy required to dissociate the molecule from potential energy minimum) and D_0 (representing the energy needed to dissociate from the molecule's lowest vibrational energy state). The horizontal lines across both potentials represent the quantized vibrational energy levels. The Morse potential accommodates a more realistic approach to molecular dissociation compared to the idealized harmonic model.

Within the harmonic approximation, the potential energy of a vibrating bond is assumed to be a perfect parabolic function with fixed spring constant regardless of the bond length (Figure S1: red curve).[2] However, the harmonic approximation becomes unreliable to quantitatively describe the vibrational behavior, especially that of the X-H bonds (for example, X = C, N, F, O etc.) due to bond anharmonicity, i.e., the deviation from the idealized harmonic oscillator model.[2] The Morse potential, in contrast to the harmonic oscillator model, offers a more precise approach by depicting a potential well that reflects the anharmonic behavior and allows for bond dissociation at longer distances (Figure S1: blue curve).[2] The quantized vibrational energy levels become closer at higher energies in the Morse potential while in harmonic potential they are equally spaced at all points in the well (Figure S1).[2]

To accurately capture the behavior of molecular vibrations in the overtone and combination bands where traditional harmonic oscillator models fall short, employing a more precise potential energy function like the Morse potential becomes essential[3,4]:

$$U(r) = D_e\left[1 - exp\left(-a(r - r_e)\right)\right]^2 \quad (1)$$

where D_e represents the dissociation energy from the bottom of the potential, r_e is the equilibrium internuclear distance, a is the Morse parameter calculated as $a = \sqrt{k_e/2D_e}$, and k_e is the force constant. [3,4] Typically, a Taylor expansion of the potential energy function, $U(r)$, can be used to extract the quadratic (harmonic) and higher order (anharmonic terms):[3,4]

$$U(r) = k_2Q^2 + k_3Q^3 + k_4Q^4 + \ldots \quad (2)$$

The terms Q^3 and Q^4, which involve higher orders beyond quadratic, are referred to as the anharmonic terms. By considering the Q^3 term, one can calculate an eigenvalue E_v:[3,4]

$$E_v = \left(v + \frac{1}{2}\right)h\nu_e - \left(v + \frac{1}{2}\right)^2 h\nu_e\chi_e \quad (3)$$

Here E_v represents the vibrational energy of the v^{th} vibrational level, v is the vibrational quantum number, h is Planck's constant, ν_e is the harmonic vibrational frequency of the bond, and $\chi_e\tilde{\nu}_e$ is the anharmonicity constant accounting for deviations from the harmonic oscillator model.[3,4] For large quantum numbers v, the vibrational energy approaches the dissociation energy D_e, $D_e = lim_{v\to\infty}E_v$, and therefore the dissociation energy D_e can be expressed as [3,4]:

$$D_e = \frac{h\nu_e}{4\chi_e} \quad (4)$$

4. Bulk Spectra

To compare our interface results with bulk properties, we performed bulk analysis using FTIR and NIR spectroscopy with a resolution of 32 cm^{-1}. This comparison is crucial for understanding the differences in vibrational characteristics between the bulk and the interface. The NIR and FTIR spectra were collected using a Perkin Elmer Spotlight 400 imaging spectrometer and a JASCO FT/IR-4700 spectrometer, respectively. For obtaining NIR spectra of liquid samples, a Harrick liquid cell with a BaF_2 window, 0.37 mm thick, was used.

The FTIR of chloroform spectrum displays a single absorption peak at 3022 cm^{-1} associated with the C-H stretch vibrations (Figure S2a: blue).[5] The NIR spectrum of chloroform exhibits an absorption band centered at 5910 cm^{-1}, representing the first overtone of the C-H stretch (Figure S2a: red).[5] Acetonitrile's FTIR spectrum shows absorption peaks at 2950 cm^{-1} corresponding to C-H symmetric stretch vibrations (Figure S2b: blue).[6] For acetonitrile, the C-H symmetric stretching vibration mode was explored as it is SFG active, whereas previous studies have shown no SFG peaks for the Fermi resonance or the methyl asymmetric stretching modes.[7-9] The NIR spectrum of acetonitrile reveals a band at 5830 cm^{-1}, corresponding to the first overtone of the C-H symmetric stretch (Figure S2b: red).[10] The FTIR spectrum of mica (Figure 4b in main manuscript: blue) reveals a distinct absorption peak at ~3633 cm^{-1}, corresponding to the O-H stretch vibrations from hydroxyl groups in the MIR region. The NIR spectrum of mica (Figure 4b in main manuscript: red) features a broad band around 7090 cm^{-1}, corresponding to the first overtone of the O-H stretch.

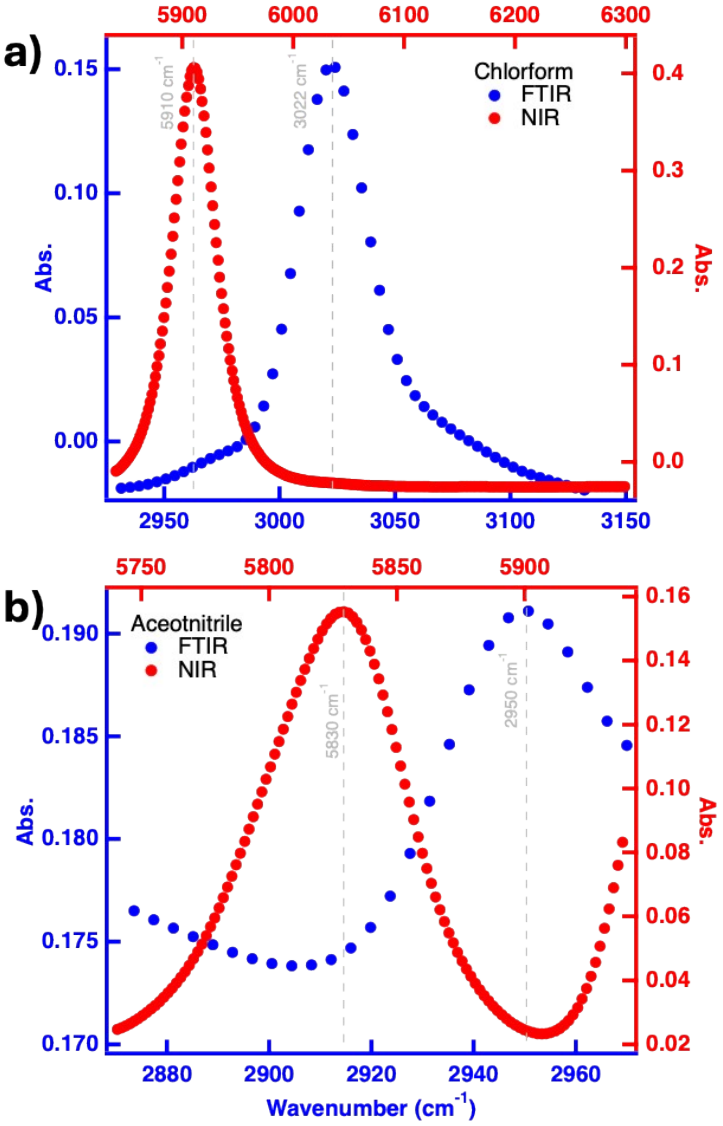

Figure S2: Bulk FTIR (blue) and NIR (red) spectra of a) chloroform and b) acetonitrile. The bottom axis (blue: FTIR) and the top axis (red: NIR) are aligned to demonstrate the overlap, with the frequency on the top axis (NIR) being twice that of the frequency of the bottom (MIR) X-axis. The gray dotted lines represent the central frequency for each observed peak at the maximum absorption.

5. Frequency Calibration

To calibrate the mid-infrared (MIR) and near-infrared (NIR) beam frequencies, we employed a specific configuration. For the MIR beam path, a thin layer of parafilm on a coverslip was introduced for the CH region (Figure S3b) while a thin piece of muscovite mica was used for the OH region (Figure S3d). In the NIR beam path, a mica film was utilized for OH overtone calibration (Figure S3f). To account for any temporal delay caused by the coverslip in the IR beam pass, a similar coverslip was positioned in the visible beam pass. The minima positions, indicated by the absorption dips shown in green traces in Figures S3b, S3d, and S3f with a small arrow, correspond to the absorption by parafilm and mica, aligning with the Fourier transform infrared (FTIR) response of parafilm (Figure S3a), as well as the FTIR (Figure S3c) and NIR (Figure S3e) responses of mica, confirming the frequency region.

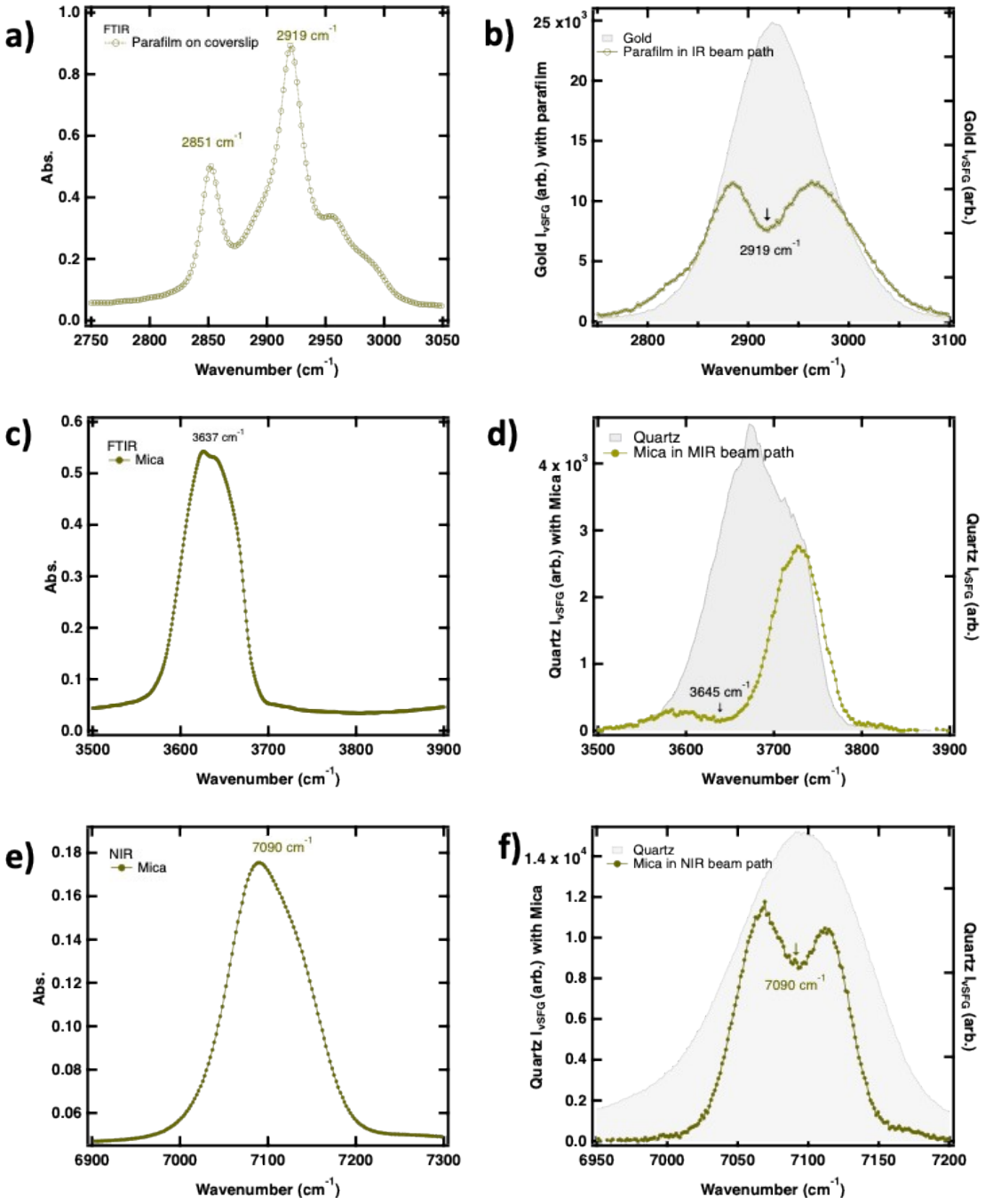

Figure S3: a) FTIR spectrum of parafilm. b) MIR-vSFG calibration spectrum with parafilm absorption dip in the CH stretching region. c) FTIR spectrum of mica. d) MIR-vSFG calibration spectrum with mica absorption dip in the OH stretching region. e) Bulk NIR spectrum of mica. f) NIR-vSHG calibration spectrum with mica absorption dip in the OH stretching overtone region. A thin layer of mica and a thin layer of parafilm placed on a coverslip was positioned in the MIR/NIR beam path. The position of the dips in b), d), and f) can be compared with the corresponding peak positions in the spectra a) and c) (FTIR), and e) (NIR), to ensure that we are at the correct IR frequency range for the experiments.

6. Fresnel Factor Correction

To obtain the molecular information in the second order hyperpolarizability tensor ($\chi_{eff}^{(2)}$), local field enhancements should be accounted. These enhancements, represented by the Fresnel factors, are incorporated by dividing the normalized vSFG spectra by the wavelength-dependent Fresnel factor. We have done Fresnel factor calculation for the α-Al_2O_3(0001)/chloroform (Figure S4a) and Al_2O_3(0001)/acetonitrile (Figure S4b) interfaces in the MIR regions. Based on our calculation, the change in the Frequency dependent Fresnel factor is flat in NIR region unlike MIR regions.

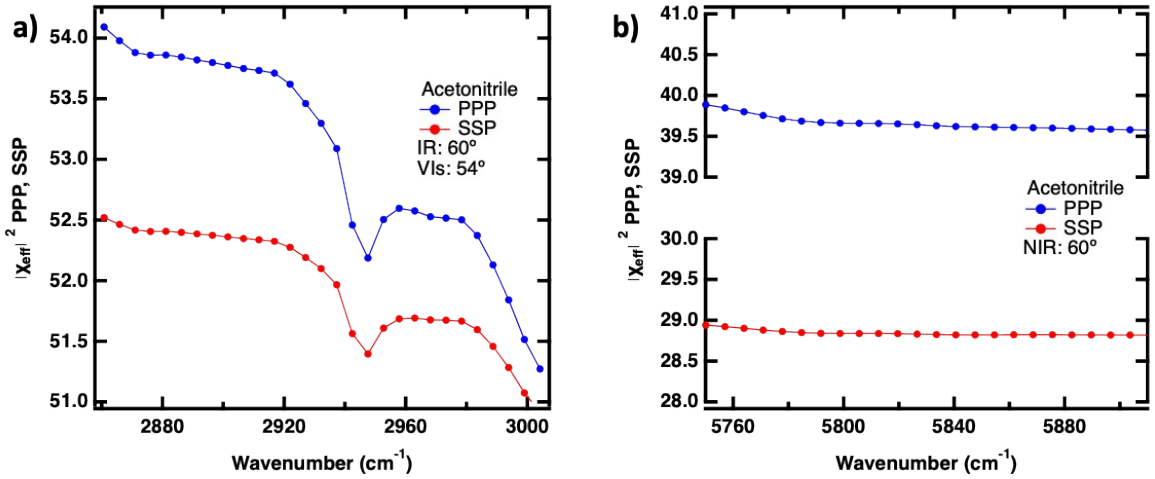

Figure S4: Frequency defendant Fresnel factors at the α-Al_2O_3(0001)/acetonitrile in the a) MIR region for the fundamental CH stretch, and b) NIR region for the CH stretch overtone. Corresponding refractive indices for the calculation is listed in Table S1.

Table S1: Refractive indices of α- Al_2O_3(0001) and Acetonitrile.

Frequency	**Refractive indices**	
	Al_2O_3 [11]	**Acetonitrile [12]**
MIR-vSFG: 793 nm	1.760	1.337
NIR-vSHG: 857 nm	1.758	1.336
Vis: 1035 nm	1.755	1.355
MIR: 3395.6 nm; (2945 cm^{-1})	1.699	1.334
NIR: 1714 nm; (5831 cm^{-1})	1.743	1.333

7. Comparing NIR-vSHG to NIR-vSFG (Selection Rule)

The similarity in the spectral features in the NIR-vSFG and NIR-vSHG responses for chloroform and acetonitrile, and flat response of the Fresnel factors in the NIR region (Figure S4) suggests a vibrational origin of the strong NIR-vSHG response. Our results unravel the intricate vibrational characteristics of higher-energy overtones using NIR-vSHG while accessing fundamental modes using the MIR-vSFG technique. By integrating these complementary approaches, a comprehensive analysis of the vibrational features can be attained, encompassing both the overtone and the fundamental vibrational modes.

While vSFG and vSHG techniques both probe vibrational transitions, they follow different selection rules. In the MIR-vSFG (left) and NIR-vSFG (middle) processes (Figure S5), incident IR and NIR pulses resonant with the system's vibrational transitions from the $\upsilon = 0$ state to the $\upsilon = 1$ and from the $\upsilon = 0$ state to the $\upsilon = 2$ state, respectively, initiate the excitation. Subsequently, a non-resonant anti-Stokes Raman process induced by a visible pulse leads to the emission of a photon at the summed frequency. This sequence of events, as visualized in the energy diagram (Figure S5), demonstrates the mechanism behind the vSFG process.

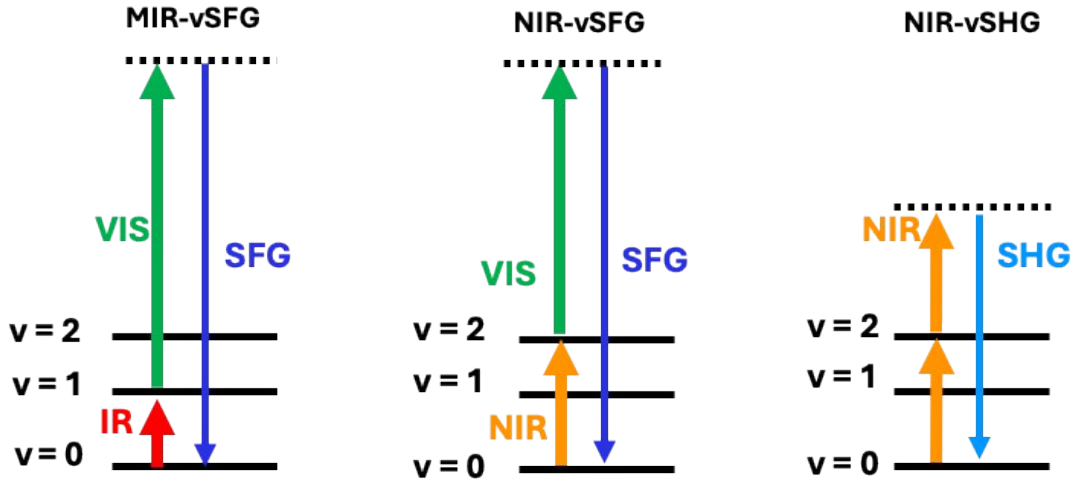

Figure S5: Energy diagram for MIR-vSFG (left), NIR-vSFG (middle) and NIR-vSHG (right) processes.

The following equation expresses the hyperpolarizability for the sum-frequency spectroscopy where the resonance enhancement occurs with one of the incident frequencies (in this case, either the MIR or the NIR beam):[13,14]

$$\beta^{ijk}(-\omega_{sum};\omega_{Vis},\omega_{(MIR\ or\ NIR)}) = \frac{-1}{2\hbar}\sum_{\upsilon}\frac{\mu_{\upsilon 0}^{k}\left(\alpha_{0\upsilon}^{ij}\right)_{AR}}{(\omega_{\upsilon}-\omega_{MIR\ or\ NIR}-i\Gamma_{\upsilon})} \quad (5)$$

where β^{ijk} is the molecular hyperpolarizability tensor, $\mu_{\upsilon 0}^{k}$ and $\left(\alpha_{0\upsilon}^{ij}\right)_{AR}$ are the IR and Raman transition matrix elements, respectively, ω_{IR} is the photon frequency and Γ_{υ} is the damping coefficient. In the following derivation, it is assumed that $\omega_{(MIR\ or\ NIR)}$ is near resonance with a particular excited state υ ($\upsilon = 1$: MIR, $\upsilon = 2$: NIR) with a transition frequency ω_{υ}, and that ω_{Vis} and ω_{sum} are far from resonance.[14,15]

In the special case of SHG when the incident beam is providing resonance enhancement at the incident frequency, the first overtone in our case, the selection rule can be derived from selection rules for the vSHG process by having the two equal incident frequencies.[14,15]

$$\beta^{ijk}(-\omega_{SHG}=2\omega;\omega_{NIR},\omega_{NIR}) = \frac{-1}{4\hbar}\sum_{\upsilon}\frac{\mu_{\upsilon 0}^{j}\left(\alpha_{\upsilon 0}^{ik}\right)_{AR}+\mu_{\upsilon 0}^{k}\left(\alpha_{\upsilon 0}^{ij}\right)_{AR}}{(\omega_{\upsilon}-\omega_{NIR}-i\Gamma_{\upsilon})} \quad (6)$$

During NIR-vSHG, an incident NIR pulse is resonant with the vibrational transition occurring from the $\upsilon = 0$ state to the $\upsilon = 2$ state (Figure S5). Subsequently, a non-resonant anti-Stokes Raman process is induced by a second NIR beam. It is important to note that the energy of the anti-Stokes Raman photon in NIR-vSHG is lower compared to those generated in the MIR-vSFG or NIR-vSFG processes. The outcome of this interaction is the emission of a photon at the summed frequency. Despite the different selection rules, as shown in equations 7 and 8 where the numerator of the $\beta^{ijk}(\omega_{SHG})$ contains a sum of two terms: $\mu_{\upsilon 0}^{j}\left(\alpha_{\upsilon 0}^{ik}\right)_{AR}$and $\mu_{\upsilon 0}^{k}\left(\alpha_{\upsilon 0}^{ij}\right)_{AR}$ reflecting contributions from different polarization components, our results suggest a

vibrational origin for the NIR-vSHG response and highlight the similarity of the technique to NIR-vSFG in probing overtones at buried interfaces.

8. vSHG & vSFG Data Fitting

The intensity of the vSFG ($I(\omega_{vSFG})$) and vSHG ($I(\omega_{vSHG})$) responses are proportional to the second order nonlinear optical susceptibility, $\chi^{(2)}_{eff}$, and the intensity of the visible and the IR beams I_{Vis} and I_{IR} in vSFG, and $(I_{NIR})^2$ in vSHG, respectively.

$$I(\omega_{vSFG}) \propto \left|\chi^{(2)}_{eff}\right|^2 I_{Vis}I_{IR} = \left|\chi^{(2)}_{NR} e^{i\varphi_{NR}} + \sum_{\nu}\chi^{(2)}_{R,\nu}\right|^2 I_{Vis}I_{IR} =$$

$$\left|\chi^{(2)}_{NR} e^{i\varphi_{NR}} + \sum_{\nu}\frac{A_\nu}{\omega_{IR} - \omega_\nu + i\Gamma_\nu}\right|^2 I_{Vis}I_{IR} \quad (5)$$

$$I(\omega_{vSHG}) \propto \left|\chi^{(2)}_{eff}\right|^2 I_{NIR}I_{NIR} = \left|\chi^{(2)}_{NR} e^{i\varphi_{NR}} + \sum_{\nu}\chi^{(2)}_{R,\nu}\right|^2 I_{NIR}I_{NIR} =$$

$$\left|\chi^{(2)}_{NR} e^{i\varphi_{NR}} + \sum_{\nu}\frac{A_\nu}{\omega_{NIR} - \omega_\nu + i\Gamma_\nu}\right|^2 I_{NIR}I_{NIR} \quad (6)$$

The vibrationally resonant modes were assumed to possess Lorentzian line shapes, where the parameters are the amplitude (A_ν), damping coefficient (Γ_ν), central frequency (ω_ν) of the ν^{th} vibrational mode, and the phase (φ) between the $\chi^{(2)}_{NR}$ and $\chi^{(2)}_{R}$. The results of the fits are shown in Table 1, Table 2 (the central frequency of the peaks) and Table 3 (peak assignments and central frequencies) in the main manuscript. The fitting parameters for the MIR-vSFG and NIR-vSHG are tabulated below in Table S2.

Table S2: Extracted fitting parameters for the PPP nonlinear optical response from the mica/air in Figure 4a by using equation S5 for MIR-vSFG and equation S6 for NIR-vSHG. ω_i, $|\chi_{NR}|$, $|A_i|$, Γ_i, φ_{NR}, *are the central frequency, amplitude, linewidth, nonresonant nonlinear susceptibility, and the phase.*

Mica/Air		
	MIR-vSFG	NIR-vSHG
$\omega_1\,(cm^{-1})$	3602.7 ± 1.2	7078.4 ± 0.4
$\omega_2\,(cm^{-1})$	3654.7 ± 1.9	7111.6 ± 0.8
$\omega_3\,(cm^{-1})$	3686.5 ± 1.9	7152.3 ± 0.9
$\lvert A_1\rvert$	1.9 ± 0.1	0.3 ± 0.1
$\lvert A_2\rvert$	2.3 ± 0.4	0.7 ± 0.4
$\lvert A_3\rvert$	0.47 ± 0.2	0.88 ± 0.1
Γ_1	25.7 ± 0.6	11.9 ± 0.5
Γ_2	40.5 ± 3.9	14.8 ± 1.6
Γ_3	20.3 ± 3.7	27.6 ± 4.3
$\lvert\chi_{NR}^{(2)}\rvert$	0.0144	-0.0011
φ_{NR}	0	0

References

[1] Direct Observation of the Orientational Anisotropy of Buried Hydroxyl Groups inside Muscovite Mica, A. Tuladhar, Z. A. Chase, M. D. Baer, B. A. Legg, J. Tao, S. Zhang, A. D. Winkelman, Z. Wang, C. J. Mundy, J. J. De Yoreo, and H.-f. Wang, *Journal of the American Chemical Society* 141, 2135 (**2019**). DOI: https://doi.org/10.1021/jacs.8b12483

[2] Anharmonicity in the Vibrational Modes Associated with H-H, N-H, O-H, and C-H bonds, S. Limpijumnong, *MRS Online Proceedings Library* 813, 361 (**2004**). DOI: https://doi.org/10.1557/PROC-813-H3.6

[3] Near Infrared Spectroscopy, L. Bokobza, *Journal of Near Infrared Spectroscopy* 6, 3 (**1998**). DOI: https://doi.org/10.1255/jnirs.116

[4] A new modified Morse potential energy function for diatomic molecules, A. M. Desai, N. Mesquita, and V. Fernandes, *Physica Scripta* 95, 085401 (**2020**). DOI: https://doi.org/10.1088/1402-4896/ab9bdc

[5] Vibrational intensities and anharmonicity in MIR, NIR and Raman spectra of liquid $CHCl_3$, $CDCl_3$, $CHBr_3$ and $CDBr_3$: Spectroscopic and theoretical study, S. Singh, R. Szostak, and M. A. Czarnecki, *Journal of Molecular Liquids* 336, 116277 (**2021**). DOI: https://doi.org/10.1016/j.molliq.2021.116277

[6] Anomalous Infrared Intensity Behavior of Acetonitrile Diffused into UiO-67, R. P. McDonnell, V. S. D. Devulapalli, T. H. Choi, L. McDonnell, I. Goodenough, P. Das, N. L. Rosi, J. K. Johnson, and E. Borguet, *Chemistry of Materials* 35, 8827 (**2023**). DOI: https://doi.org/10.1021/acs.chemmater.3c00639

[7] Theoretical and experimental examination of SFG polarization analysis at acetonitrile–water solution surfaces, K. Saito, Q. Peng, L. Qiao, L. Wang, T. Joutsuka, T. Ishiyama, S. Ye, and A. Morita, *Physical Chemistry Chemical Physics* 19, 8941 (**2017**).

[8] Influence of High pH on the Organization of Acetonitrile at the Silica/Water Interface Studied by Sum Frequency Generation Spectroscopy, B. Rehl, Z. Li, and J. M. Gibbs, *Langmuir* 34, 4445 (**2018**). DOI: https://doi.org/10.1021/acs.langmuir.7b04289

[9] Structure and Dynamics of Acetonitrile at the Air/Liquid Interface of Binary Solutions Studied by Infrared−Visible Sum Frequency Generation, J. Kim, K. C. Chou, and G. A. Somorjai, *The Journal of Physical Chemistry B* 107, 1592 (**2003**). DOI: https://doi.org/10.1021/jp021227e

[10] Chemical composition determination of complex organic-aqueous mixtures of alcohols, acetone, acetonitrile, hydrocarbons and water by near-infrared spectroscopy, M. V. Reboucas, D. S. Brandão, A. Trindade, M. F. Pimentel, and L. S. G. Teixeira, *Vibrational Spectroscopy* 55, 172 (**2011**). DOI: https://doi.org/10.1016/j.vibspec.2010.11.003

[11] Refraction and Dispersion of Synthetic Sapphire, I. H. Malitson, *J. Opt. Soc. Am.* 52, 1377 (**1962**). DOI: https://doi.org/10.1364/JOSA.52.001377

[12] Refractive, dispersive and thermo-optic properties of twelve organic solvents in the visible and near-infrared, K. Moutzouris, M. Papamichael, S. C. Betsis, I. Stavrakas, G. Hloupis, and D. Triantis, *Applied Physics B* 116, 617 (**2014**). DOI: https://doi.org/10.1007/s00340-013-5744-3

[13] Sum Frequency Generation of Acetonitrile on a Rutile (110) Surface from Density Functional Theory-Based Molecular Dynamics, S. Luber, *The Journal of Physical Chemistry Letters* 7, 5183 (**2016**). DOI: https://doi.org/10.1021/acs.jpclett.6b02530

[14] A Unified Treatment of Selection Rules and Symmetry Relations for Sum-Frequency and Second Harmonic Spectroscopies, A. J. Moad and G. J. Simpson, *The Journal of Physical Chemistry B* 108, 3548 (**2004**). DOI: https://doi.org/10.1021/jp035362i

[15] Sum-frequency vibrational spectroscopy of the solid/liquid interface, C. D. Bain, *Journal of the Chemical Society, Faraday Transactions* 91, 1281 (**1995**). DOI: https://doi.org/10.1039/FT9959101281